Fiber-coupled nuclearized raman probe for remote gas monitoring in nuclear containment: proof-of-concept for h2-risk management of design & beyond-design accidents

Sylvain Magne, Ahmed Bentaib, Leroy Matthieu, Emmanuel Porcheron, Etienne Studer, Nabiha Chaumeix, Audrey Ruffien-Ciszak, Julien Dhote

FIBER-COUPLED NUCLEARIZED RAMAN PROBE FOR REMOTE GAS MONITORING IN NUCLEAR CONTAINMENT: PROOF-OF-CONCEPT FOR H_2-RISK MANAGEMENT OF DESIGN & BEYOND-DESIGN ACCIDENTS

Sylvain Magne[1], Matthieu Leroy[1], Ahmed Bentaïb[2], Emmanuel Porcheron[3], Etienne Studer[4], Nabiha Chaumeix[5], Audrey Ruffien-Ciszak[6], Julien Dhote[6]

[1] Université Paris-Saclay, CEA, List, F-91120 Palaiseau, FRANCE.
[2] IRSN, PSN-RES/SAM, BP17, F-92262 Fontenay-aux-Roses, FRANCE.
[3] IRSN, PSN-RES/SCA, BP68, F-91400 Saclay, FRANCE.
[4] CEA/DES/ISAS/DM2S/STMF/LE2H, CEA/SACLAY, F-91191 Gif-sur-Yvette, FRANCE.
[5] Institut ICARE, 1C Route de la recherche scientifique, F-45071 Orléans, FRANCE.
[6] ARCYS, 14 Place Marcel Dassault, F-31700 Blagnac, FRANCE.

(E-mail: sylvain.magne@cea.fr, ahmed.bentaib@irsn.fr, emmanuel.porcheron@irsn.fr, etienne.studer@cea.fr, chaumeix@cnrs-orleans.fr, julien.dhote@arcys.fr)

ABSTRACT

During the course of a severe accident (SA) in a Light Water Reactor (LWR), large amounts of hydrogen (H_2) gas are likely to be generated and released into the containment during core degradation, potentially raising a combustion hazard. Additional burnable gases (H_2 and CO) may be released into the containment volume in case of Molten Corium/Concrete Interaction (MCCI).

Within the extension period of the MITHYGENE Project, CEA LIST, IRSN and ARCYS have designed, assembled and tested a fiber-coupled nuclearized gas prototype probe, based on optical Raman technology, and complying with the specifications of a severe accident. This monitoring technique conveys many decisive advantages such as chemical-selective, distributed and local gas measurement (cm^3). It aims at providing *in situ* accurate information on gas mixture (H_2, O_2, N_2, steam, CO, CO_2) in quasi real-time and in several locations inside the containment and the annulus. Compared to the previous Raman probe developed within the first period of the MITHYGENE Project, this new Raman probe is more efficient and includes improved functionalities such as polarization-diversity Raman measurements and anti-fogging anti-aerosol device with the aim to prevent both water condensation and aerosol deposition. Two algorithms are evaluated to compensate for Cerenkov perturbations (background subtraction and polarization correction). We describe experimental qualifications performed in the NC2V gas cell (CNRS-ICARE) and in the IRMA irradiation cell (IRSN).

The MITHYGENE Project ends up with a proof-of-concept of Raman probe dedicated to H_2/MCCI-risk management. The Technological Readiness Level (TRL) of the prototype probe is between 5 and 6.

KEYWORDS: FIBER OPTICS, HYDROGEN, MCCI, MONITORING, RAMAN, SAMGs, SEVERE ACCIDENT

1. INTRODUCTION

During the course of a severe accident (SA) in a Light Water Reactor (LWR), large amounts of hydrogen (H_2) gas are likely to be generated and released into the containment during core degradation [1-4]. Additional burnable gases (H_2 and CO) may be released into the containment volume in case of Molten Corium/Concrete Interaction (MCCI). This could subsequently raise a combustion hazard causing high-pressure peaks that could challenge the reactor containment and lead to the failure of surrounding equipment. A H_2 explosion may also be of safety concern to spent fuel storage areas, where flammable conditions may be reached if adequate ventilation is not provided. In this case, a H_2 explosion may lead to the dispersion of radioactive products into the environment (Fig. 1).

Core melting accidents in Nuclear Power Plants (NPPs) occurred twice in history: in Three-Mile Island (USA) in 1978, and in Fukushima-Daïchi (Japan) in 2011 [5], respectively rated INES 5/7 and 7/7 (International Nuclear and radiological Event Scale). Within the first hour following the onset of the accident, the temperature may rise up to 170°C into the containment and its internal pressure may reach 9 bar (0.9 MPa). Meanwhile, the ambient dose rate may be as high as 1 kGy/h and the relative humidity may reach 100 % (saturated water vapor condition) in a highly basic environment (pH ~ 9.2) due to potential presence of soda. In the same time, airborne particles (aerosols) are dispersed into the inner volume as well. Several hours later, the dose rate is expected to drop due to the fall of fission products onto the concrete floor. Several weeks after the accident, the cumulated dose is estimated to be around 2 MGy. This value accounts for both the operational dose (integrated over the lifetime of the NPP) and the accidental dose.

Dedicated mitigation strategies (NPP design-dependent) usually combine the implementation of safety components (*e.g.* Passive Autocatalytic Recombiners (PARs)) and the definition of adequate Severe Accident Management Guidelines (SAMGs) [1-4]. In the French Pressurized Water Reactors (PWRs), SAMGs rely on data (pressure, core exit temperature, dose rate) provided by limited monitoring devices. The gaseous composition of the containment atmosphere is not monitored and only PARs located on polar crane are equipped with thermocouples to detect H_2 through the heat released by the exothermic recombination reaction with O_2. Therefore, PARs only provide a mitigation of the H_2-risk and cannot assess for it. Furthermore, studies by IRSN led to the conclusion that the recombination rate of H_2 by PARs may be much less than the generation rate, particularly during the first hours of the accident. Finally, aerosol particles released during the accident in addition to some gases (CO, I_2, CH_3I…) may poison PARs.

The assessment of both deflagration and detonation risks is obtained by plotting pressure data of H_2, air and water vapor onto a three-component diagram (Shapiro-Moffette ternary diagram) [6] (Fig. 2). The measurement of partial pressures of H_2, O_2, N_2 and H_2O in several locations inside the containment is therefore required to fully assess for the H_2-risk. The readout time must be less than 10 minutes, in accordance with SAMGs. Furthermore, the monitoring of additional gases such as CO and CO_2 provides complementary information about MCCI.

To date, two gas measurement techniques, based on gas sampling [7] and catalytic sensors [8], are implemented in some NPPs. Both technologies have drawbacks and limitations.

The use of catalytic sensors leads to wrong H_2 estimation in case of gas temperature stratification, in case of lack of oxygen or in the presence of CO. Catalytic sensors only detect H_2, so data are missing to fully assess for the H_2-risk.

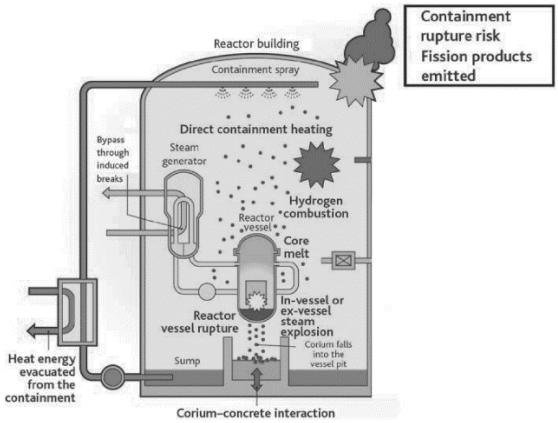

Figure 1. ***Consequences of a core-melt accident in a reactor building, from [2]***

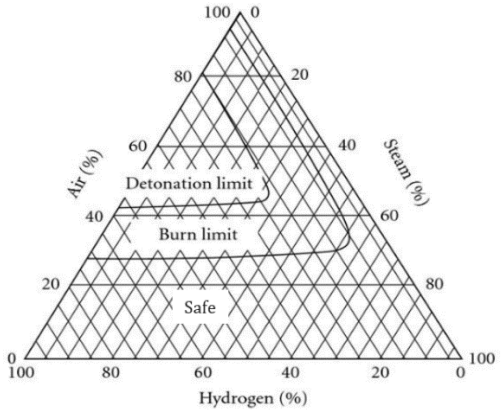

Figure 2. ***Shapiro-Moffette diagram (H_2-H_2O-air), from [6]***

Overheated sampling pipes transport gas samples out of the concrete barrier into a monitoring module installed outside, able to detect all gases of interest for assessing the H_2-risk [7]. However, the estimation of partial pressures may be strongly biased because of gas segregation onto the internal pipe surface. Moreover, both gas transport and analysis impose a significant delay time in contradiction with the need to react quickly and to provide reliable data about gas mixture flammability status to the operator and safety authorities at early times of the accident (*i.e.* within the first ten minutes).

As the French safety doctrine precludes gas extraction for sake of containment tightness, an *in-situ* distributed multigas sensing device that overcomes the catalytic sensors limitations is needed to provide reactor operators with relevant information about containment gas mixture composition and eventually to estimate deflagration/detonation risks, by a suitable identification onto the ternary diagram.

2. REMOTE MONITORING USING FIBER-COUPLED GAS PROBES

Unlike previous techniques, optical-based techniques mainly involve absorption or Raman scattering spectrometry. In a highly radiative environment, only the near infrared (NIR) range of the optical spectrum is suitable for light transmission through optical fibers. In this optical range, the absorption technique is not well suited to symmetric molecules such as N_2 and H_2 because useful optical transitions are very weak [9] therefore requiring very long interaction lengths to compensate for lesser efficiency, in contradiction with the requirement for a localized measurement.

Unlike the absorption technique, all molecules of interest for the H_2-risk assessment (H_2, O_2, N_2, H_2O, CO, CO_2) exhibit efficient Raman signatures [10-11]. In this study, all species of interest are light molecules of large Raman Stokes shifts, ranging typically from 785 cm^{-1} (H_2) up to 3657 cm^{-1} (H_2O), making discrimination easier with compact grating-based spectrometers or conventional bandpass filters.

For all species of interest, Table 1 shows the Raman shifts (in cm^{-1}), Raman wavelengths (for a laser wavelength of 750 nm), and the relative Raman cross-sections with respect to nitrogen. All transitions are vibronic in nature except H_2 (S_1), which is rotational.

Fig. 3 shows the reconstructed Raman spectrum for all gases of interest in this study. All Raman peaks are well separated from each other; no interference is observed between species. It is worthwhile noticing that water vapor (a ubiquitous interfering gas in FTIR spectrometry) is well discriminated against the other gases.

Gas	σ/σ_{N2}	$\Delta\nu$ (cm^{-1})	Depolarization ratio ρ (%)	λ Raman (nm)
H_2 (S_1)	2.4	587	75	785
CO_2	1.3	1285 and 1388	~4 to 5	830 and 837
O_2	1.2	1556	~3	849
CO	1	2145	~0.6	894
N_2	1	2331	~1	909
H_2O	3.2	3657	~0.03	1033

Table 1: ***Raman shifts, wavelengths (@750 nm) and relative cross-sections vs. N_2 (data from [12-15])***

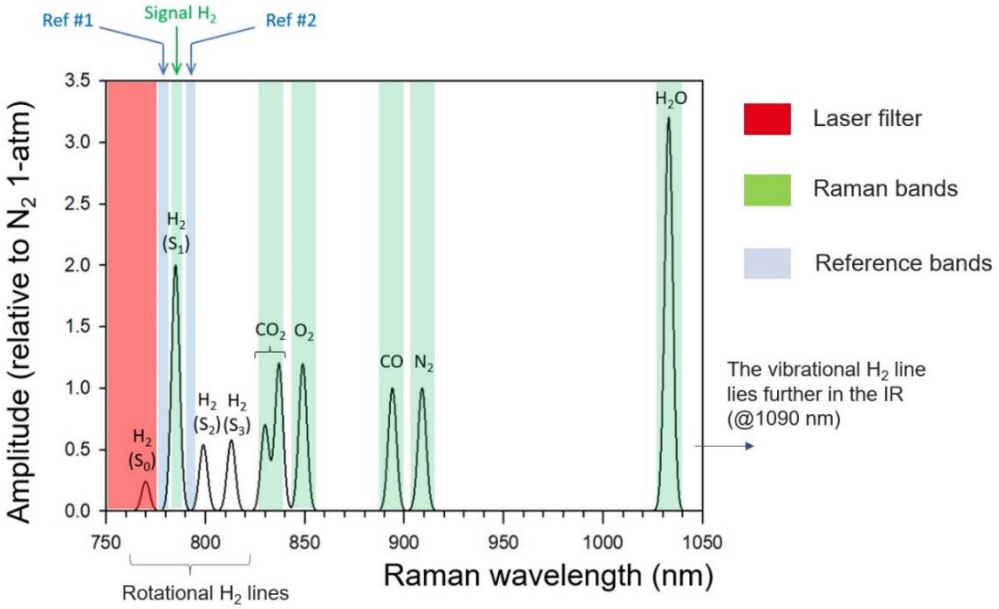

Figure 3. ***Reconstructed Raman spectra for all gases of interest for H_2-risk assessment. The amplitudes are normalized to that of N_2.***

The Raman signal S is proportional to laser intensity (I_{laser}, in W/m^2) and integration time t according to the following relation [16]:

$$S \cdot T = K \cdot I_{Laser} \cdot \sigma \cdot \Delta\Omega \cdot \mathrm{P} \cdot \mathrm{t} \qquad (1)$$

where T (in K) and P (in Pa) are the temperature and the partial pressure of the gas respectively, $\Delta\Omega$ is the solid angle of observation, σ is the Raman cross-section of the gas and K is a gas-dependent calibration constant.

It turns out from Eq. (1) that the temperature T of the gas mixture must be known in order to determine the partial pressure P. Furthermore, it is also necessary to known the absolute pressure P_{tot} inside the containment volume to determine the relative gas concentration P/P_{tot}. The control-command of the NPP actually provides a pressure measurement. An additional SA-qualified temperature sensor must be incorporated into the probe, close to the laser focus point.

For main gases listed in table 1, the depolarization ratio (*i.e.* ratio of perpendicular to parallel elements of the electric vector of Raman light) is of the order of several percents or even less. It means that the

main contribution of scattered Raman light is highly polarized and has an electric vector aligned with that of the laser beam (*i.e.* for N_2, the unitary Raman electric vector is typically (0.99995, 0.01). By contrast, the depolarization ratio of the rotational Raman signal of H_2 is 75 % which means that the rotational Raman signal of H_2 is depolarized and its unitary electric vector is expected to be (0.64, 0.48). Although many fiber-coupled Raman gas probes are already available on the market (Kaiser, In-Photonics, Axiom, Horiba, to name a few), they do not comply with SA specifications and cannot be qualified "as is". Immersion Raman probes are convenient for process monitoring due to their low intrusiveness. A unique lens serves to focus the high-pass filtered laser light and to collect the Raman light, both signals being separated by a dichroic filter embedded into the probe.

The Raman analysis of gas mixtures is more challenging than the Raman analysis of solids and liquids because the density of gases is about three orders of magnitude less. The residual laser light, as well as unwanted Raman or fluorescence contributions, must be heavily filtered out. Fortunately, Raman spectra of gases appear as narrow bands, thus facilitating the discrimination *vs.* background. Moreover, the backscattered Raman light from most gases of interest is highly polarized (as explained before), making it possible to modulate the Raman signal by rotating a polarizer. Polarization-rotation thus provides a first means to discriminate Raman signals from other polarization-independent light perturbations such as fluorescence from disordered solids or Cerenkov light. Furthermore, the Raman signal may be modulated by tuning laser intensity. This provides a second means to discriminate laser-driven signals (Raman, fluorescence) from exogenic signals (*e.g.* Cerenkov).

Finally, as the quantum efficiency of most NIR photon detectors (silicon junctions or GaAs photocathodes) dramatically drops with increasing wavelength, short-wavelength lasers are usually advocated for Raman spectrometry (typically 532 nm). Exception to this rule is made when fluorescence is suspected and, in this special case, a very common laser wavelength is 780 nm. A list of references of some past developments is provided in [16].

It is worthwhile noticing that Raman spectrometry is EXAT-compatible (EXplosive ATmosphere). This monitoring technique has indeed already been demonstrated in EXAT environments, for instance in a gas turbine power plant [17], with a 5-W laser operating at 532 nm. The Minimum Ignition Energy (MIE) for H_2-ignition in air depends on relative concentrations of H_2, O_2 and N_2. At a pressure of 1 atm, a minimum value of 6 µJ is found at a H_2 concentration of 30% and a ratio $O_2/(O_2+N_2)$ of 35% [18]. The MIE is standardly determined by capacitive spark discharge of less than 100 ns duration. Therefore, the minimum discharge power is of the order of 60 W, *i.e.* much higher than usual laser power (another way to get to the same conclusion is to consider the amount of energy delivered by the laser beam during 100 ns, which is far less than the MIE).

The optical fibers used for Raman light collection are multimodal (MM), commonly selected on account on their high *étendue* (throughput) in order to maximize the collection of Raman signal. The *étendue* is proportional to the product of the solid angle by the core surface. Large core diameter fibers are recommended in order to improve light collection. However, the flexural rigidity also increases with the third power of diameter. This imposes a limit in the radius of curvature (typically 20 cm for a 600-µm diameter fiber) so as to minimize bending-induced stress and to ensure long-term safe operation. As a result, a compromise must be found between collection efficiency and mechanical flexibility for fiber deployment and internal connections inside the probe.

The fibers are usually coated with thermoplastics polymers. Polyimide is often used on account on its temperature and radiation hardness. The fibers are inserted into a metallic sheath covered by a black polymer providing water- and light-tightness. SMA or ST connectors are also often used.

3. CHALLENGES ASSOCIATED WITH AN IN SITU REMOTE RAMAN GAS MONITORING TECHNIQUE FOR SA MONITORING

When used in the particular conditions of a nuclear accident, the main limitations arise from Radiation-Induced Emission (RIE), Radiation-Induced Attenuation (RIA), water condensation and aerosol pollution. Let us describe in more details each perturbation.

Radiation-Induced Emission (RIE)

RIE is composed of Radioluminescence (RL) and Cerenkov light.

A Cerenkov Effect occurs when charged particles (essentially electrons) travel faster than the speed of light in the material. In silica glass (refractive index ~ 1.46), the energy threshold is 180 keV. It manifests itself as an emission of a broadband and depolarized continuum light emission. The Power Spectral Density (PSD in W/nm) of the Cerenkov spectrum evolves as the inverse third power of wavelength ($1/\lambda^3$ trend). As far as photon-counting devices (*e.g.* photomultipliers or Charge-Coupled Devices (CCDs)) are involved, the photon flux evolves as the inverse double power of wavelength, *i.e.* according to a $1/\lambda^2$ trend [19]. Since the Raman scattering cross-section is decreasing with laser wavelength λ_I according to the well-known $1/\lambda_I^4$ law, the ratio Cerenkov/Raman changes as a function of $1/\lambda_I^2$, therefore motivating the use of short-wavelength lasers. However, the Radiation-Induced Attenuation (RIA) in silica fibers increases dramatically at shorter wavelengths as well. Because of this, the most appropriate laser wavelength is the result of a compromise between Raman detection efficiency and RIA. In this study, the laser wavelength was 750 nm.

As an example, at the wavelength of 870 nm (mid-Raman range), we recorded a PSD of 21 fW/nm for a 5-m long exposed fiber exposed under a dose rate of 5 kGy/h [16]. The normalized PSD is then about 0.78 $fW.nm^{-1}/(kGy/h)$ per meter of fibre, in accordance with published data [19]. The Cerenkov signal generated by a 10-meter long collection fiber exposed to a dose rate of 1 kGy/h is 2 to 3 orders of magnitude higher than Raman signals of the gases of interest.

RL also occurs in silica fibers in specific bands, especially at 660 nm [20]. Aside from this spectral band, the Cerenkov Effect is the dominant perturbation.

Previous developments within the MITHYGENE Project has led to the design and test of a compact proprietary Raman probe that relied on single-pass transverse Raman collection [16]. This probe successfully passed all the trial tests except the radiation one. Although we performed this test in air, we estimated the Maximum Tolerable Dose Rate (MTDR) for a 10 hPa (1 %) H_2 resolution (1-σ unity SNR), based on the conversion coefficient between H_2 and N_2 Raman signals (obtained in shock tube experiments [16]). We got to the conclusion that the MTDR was about 14 Gy/h for an integration time of 5 minutes and an exposed fiber length of 5 meters [16], which of course did not comply with SA specifications. This motivated us to design an improved Raman probe of higher efficiency and selectiveness *vs* Cerenkov light.

Radiation-Induced Attenuation (RIA)

Light is guided by internal reflection inside the fiber core, surrounded by a thin cladding of lesser refractive index. Radiation-hard fibers are pure silica-core and fluorine-doped fibers. Fluorine is a dopant used to lower the refractive index of silica and as such, is mostly used in cladding composition (optionally in core composition). In the red part of the visible spectral domain, the RIA mainly stems from the Non-

Bridging Oxygen-Hole Centers (NBOHC), which transition peaks around 640 nm (FWHM ~80 nm). Taking into account all previous data, we chose the laser wavelength in the range [730 nm – 750 nm].
RIA in fibers is a complex phenomenon [21]. Only photon interaction is considered here (neutron interaction is negligible in both operational and accidental conditions). High-OH fibers are known to better recover under radiation but a high-order OH absorption harmonics lies in the expected laser range of [730 nm – 750 nm]. Consequently, we considered anhydroguide (low-OH) fibers in view of radiation tests (Polymicro FIP-400 and FIP-600, purchased from *SEDI Fibres Optiques* (France)).

Water condensation

Water condensation arises when water vapor condensates onto a coldest surface. Liquid water droplets deposited onto an optical window contribute to scatter light out and prevent its efficient collection. This situation is actually expected to happen at early times (first hour) of an accident when water vapor (leaking out from the reactor core) is hotter than the probe. To prevent this, Joule heating usually heats up optical components during the first hours of the accident. Although this requires Ampere-like currents, the energy involved is manageable by portable batteries because the time delay before temperature inversion (*i.e.* when water vapor gets colder than the probe) is of the order of the hour.

Airborne particles (aerosols)

During a core-melt accident, airborne particles are likely to be released into the containment volume. The aerosols may be composed of soot (due to combustion of plastic sheaths), fission products (RbI, etc.), metallic (Fe-, Cr-, Si-, Al-, Mg-, Ni-, Sn- and Zr-oxide particles are released) and nuclear fuel residuals (due to core degradation, *e.g.* U). The size distribution of core-melt produced particles is usually estimated using cascade impactors. In addition, MCCI generates compounds of sodium, potassium, magnesium and calcium originating from concrete degradation [22].
IRSN previously studied Raman spectrometry in presence of aerosols, under thermal SA-representative hydraulic conditions in a reactor containment facility [23-24]. In these studies, the probe was placed away, out of the gas cell, remotely collecting Raman light with the help of a long focal-length objective. Therefore, the optical components of the probe were not contaminated. This experiment revealed that aerosol particles actually increase Mie scattering without having significant impact on Raman signals because the laser filter efficiently removes the scattered light.
Conversely, Raman probes designed within the MITHYGENE Project are doomed to face direct aerosol exposure. With the aim to investigate a potential aerosol perturbation, an experimental study was performed in ambient air, with the compact probe developed within the first part of the MITHYGENE Project [16], surrounded by aerosols dispersed from submicrometric SiC solid particles [25]. We were able to recover the Raman signals of O_2 and N_2 in presence of aerosols although we noticed changes in the baseline and calibration coefficients possibly due to additional unwanted fluorescence resulting from contamination of optical parts. It is therefore essential to prevent aerosols from accumulating onto optical parts.

Within the MITHYGENE Project, CEA LIST, IRSN and ARCYS have designed, assembled and tested an improved version of fiber-coupled nuclearized gas prototype probe, based on optical Raman technology, and complying with SA specifications. It aims at providing *in situ* accurate information on gas mixture (H_2, O_2, N_2, steam, CO, CO_2) in quasi real-time and in several locations inside the containment and the annulus.

4. DESCRIPTION OF THE RAMAN INSTRUMENTATION

4.1. Description of the nuclearized Raman probe

The nuclearized Raman probe designed, assembled and tested during the extension part of the MITHYGENE Project is shown on Fig. 4. All optical devices are mounted onto a base plate, itself mounted inside a sealed case (Hoffman HSDH161608SS, 406 x 406 x 203 mm^3, IP69K). The Raman probe may be filled with air, with a neutral gas (*e.g.* argon), or with a reference gas (*e.g.* CH_4) through a vent plug. The probe is equipped with two optical penetration assemblies (SEDI KTRAV M10) allowing for laser input (laser fiber) and Raman signal output (Raman collection fiber). Two additional electrical penetrations (Swagelok fit filled with high-temperature epoxy) are also installed in order to transmit both heating current and electric command for polarization rotation through silicone-coated wires.

Since the State Of Polarization (SOP) is not maintained in a MM fiber, the laser light incoming from the laser fiber (400 µm diameter, NA ~ 0.22) is first polarized through a polarization beam splitter (PBS) cube (Thorlabs PBS 12-780-HP). At the output of the PBS, the electric vector of the laser light is aligned parallel to the support base. Afterwards, the laser light is low-pass filtered (Thorlabs FESH0800 and two Semrock FF01-766/13-25) in order to remove unwanted light contribution in the Raman band. All filters exhibit seven orders of magnitude attenuation in the stop band. Then, after being reflected by a beamsplitter (BS) plate (Semrock FF01-776/LP-25) set at 20° incidence, it is focused out of a fused silica window with the help of a parabolic mirror (Thorlabs MPD149-M01). The silica window is 4-mm thick and oriented at Brewster angle (~ 56°) in order to avoid back reflection. The focal point is located at about 15 mm away from the external window surface. Laboratory experiments performed with and without Brewster window show similar Raman spectra, evidencing for low impact of the window.

In Fig. 4a, both laser and Raman beams are shown in the plane of the figure, for sake of clarity. However, in the real probe, the beams are projected through the base plate, as shown in Fig. 4b-4c-4d.

The gas mixture is enclosed with an anti-fogging and anti-aerosol (AF-AA) module that is fixed onto the probe surface and encompasses the Brewster window. The probe is also meant to be vertically fixed onto a wall with spring-compensated supports. This will allow to keep the AF-AA module protected in between the probe and the wall. The laser beam interacts in the AF-AA module horizontally, while the gas is ascending through the module by natural convection. Joule heating is delivered within the AF-AA by winding a silicone-coated Constantan wire (resistivity ~ 30 Ohm/m)). In practice, the maximum heating is obtained when the resistance of the remote connection is equivalent to the resistance of the Constantan wire, which is 3 Ohm in our case. A current of 4 A under 24 V is required to achieve anticondensation in accidental conditions.

The Raman light generated at the focal point is collected by the same parabolic mirror and sent back to the internal part of the probe. It propagates through the BS plate, a low-pass filter removing excess laser light (Semrock FF01-776/LP-25), a rotating polarizer, and is eventually focused into the Raman collection fiber (600 µm diameter, NA ~ 0.22). A fiber core diameter of 600 µm leads to a FWHM of 8 nm (Fig. 3). The rotating polarizer is mounted inside a 20-teeth gear wheel, actuated by a 40-teeth gear wheel mounted onto a 45° ElectroMagnetic (EM) rotator (Saia-Burgess, 40 W, 28 V). A 45°-turn of the EM rotator then switches the polarizer by 90°.

The filters are mounted into rotating supports blocked at optimized angle. The supports are tuned so as to get close to full laser extinguishing while keeping laser power high enough (the larger the angle between the laser beam and the surface normal, the lower the cut-off wavelength). The same procedure is applied to the low-pass filter. The Raman spectrum starts from 772 nm, up to 1050 nm.

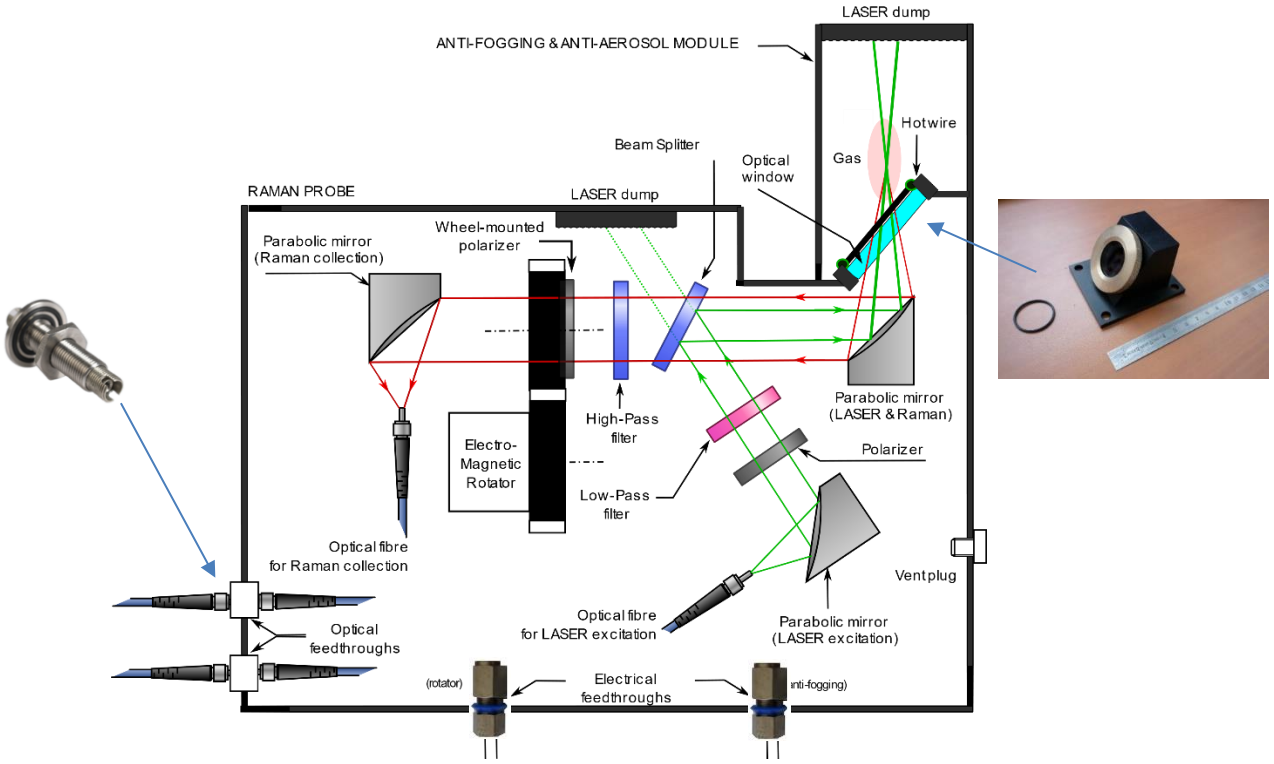

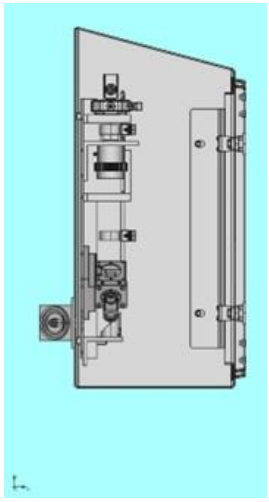
b/

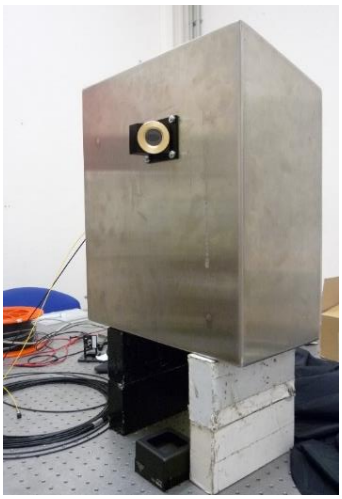
c/


d/

Figure 4. ***View of the Mithygene nuclearized Raman probe (without AF-AA module) (a/ scheme, b/SolidWorks design (Dassault Systèmes, France) c/ external view, d/ top view***

The AF-AA module is also equipped with a black-painted labyrinth that enables gas propagation (driven by convection) while preventing external light to come in. Conversely, this module also serves to block the laser light after the focus point, in compliance with eye safety procedures.

This AF-AA module was not used for laboratory experiments because we had to leave free access to the window to accommodate gas samples (TEDLAR bags). Because of this, the Raman experiments were conducted in dark room, protected by a dark blanket.

4.2. Description of the Raman spectrometer rack

A mobile rack incorporates a laser diode module (Frankfurt Laser Co., FLC300, @750 nm, 3.5 W, SMA905 output), an imaging spectrometer (ANDOR Shamrock 193i, 193-mm focus, F/3.6) equipped with a silicon-based ultra-low noise Charge-Coupled Device (CCD iDUS416A-LDC-DD), a laptop running the SOLIS software (ANDOR) and ancillary electronics (power supplies, switch trigger for the EM rotator). The CCD detector provides pictures of 2000 x 256 pixels (16 bits = 65 536 datacounts (Cts)). Each pixel covers about 0.15 nm. The CCD is cooled down at -75°C and exhibits a very low dark noise of ~ 0.01 e-/pix/s. The quantum efficiency of silicon dramatically drops beyond 1000 nm. In practice, a better statistics is obtained by integrating the entire Raman band.

4.3. Algorithms for Raman discrimination against fluorescence and Cerenkov perturbations

Raman signals of main gases of interest are both laser power- and polarization-dependent. Tuning laser power makes it possible to discriminate Raman signal from Cerenkov light. Similarly, by rotating the SOP, it is possible to discriminate Raman signals from both Cerenkov light and internal fluorescence/Raman light coming from optical parts.

Algorithm #1: Polarization correction (PC)

Let us define ϑ=0° as the pass-through angle (polarization axis aligned along the laser electric vector, *i.e.* parallel to plane surface) and ϑ=90° (high-attenuation angle), we proceed to a first spectrum recording for ϑ=0°, immediately followed by a second one at ϑ=90°.

We then make the difference between both signals, as follows

$$S_{corr}(\lambda) = (S_{0°}(\lambda) - DN) - ratio(\lambda) * (S_{90°}(\lambda) - DN) \quad (2)$$

where $S_{corr}(\lambda)$ is the corrected Raman spectrum, $S_{0°}(\lambda)$ and $S_{90°}(\lambda)$ are the raw Raman spectra for 0° and 90° orientations, respectively. Out of Raman bands (*i.e.* on baseline), $S_{corr} = 0$ and then the calibrated spectral ratio ratio(λ) writes as follows:

$$ratio(\lambda) = \frac{S_{0°}(\lambda) - DN}{S_{90°}(\lambda) - DN} \quad (3)$$

where DN is the dark noise of the CCD.

The CCD noise includes the dark noise (properly speaking) and the readout noise, associated with charge transfer for recording. The readout noise is actually the dominant noise source. It must be minimized by limiting the number of readouts (ideally only one). However, when the CCD detector is over-exposed, it may reach saturation in a short amount of time, thus leading to unusable data. In order to make sure that channel counts remain below 65 536 (16 bits), it is necessary to reduce the readout time accordingly. Long integration times are then achieved by accumulating multiple readouts and the readout time must be carefully controlled for noise optimization.

The spectral ratio takes into account the polarization dependence of the background signal. It must be calibrated separately early before Raman recordings. In practice, it is not necessary to vacuumize the probe head, this calibration being done in air. Once the spectral ratio function is calculated, O_2 and N_2 lines are eliminated in order to keep the baseline only. Finally, the resulting spectral function is fitted (most often to a straight line, §6.4).

Let us get more into the details of this first algorithm when both fluorescence and Cerenkov light are present and must be discriminated against. The action of rotating the polarizer actually gives rise to two fluorescence data ($F_{0°}$ and $F_{90°}$) and two Cerenkov data ($C_{0°}$ and $C_{90°}$). Although the Cerenkov light is fully depolarized, $C_{0°}$ and $C_{90°}$ are slightly different due to light transmission through the probe.

The Raman signal R that is inferred from this algorithm is actually the difference between parallel (0°) and orthogonal (90°) contributions. As the orthogonal contribution may be neglected for most gases (except H_2), the resulting Raman difference is of same order as the parallel contribution.

In the end, there are five unknown parameters: R, $F_{0°}$, $F_{90°}$, $C_{0°}$ and $C_{90°}$. We therefore need five equations to identify those five signals incoming onto the CCD.

The first equation is Eq. (2), linking $F_{0°}$ to $F_{90°}$. Let us describe the four remaining equations.

When the laser is OFF (no laser emission), both Raman and fluorescence lights are turned off as well and the Cerenkov light is the only signal present.
Therefore, when the polarizer is oriented along 0°, we get: $S_1(\lambda) = C_{0°}(\lambda) + DN$ (4)
And when the polarizer is oriented along 90°, we get: $S_2(\lambda) = C_{90°}(\lambda) + DN$ (5)
Then, when the laser is turned on, the Raman and fluorescence signals are superimposed over the Cerenkov light. Similarly, when the polarizer is oriented along 0°, we get:

$$S_3(\lambda) = R(\lambda) + F_{0°}(\lambda) + C_{0°}(\lambda) + DN = R(\lambda) + F_{0°}(\lambda) + S_1(\lambda) \quad (6)$$

And when the polarizer is oriented along 90°, we get:

$$S_4(\lambda) = F_{90°}(\lambda) + C_{90°}(\lambda) + DN = F_{90°}(\lambda) + S_2(\lambda) \quad (7)$$

Making the difference between Eq. (6) and (4), we get: $S_3(\lambda) - S_1(\lambda) = R(\lambda) + F_{0°}(\lambda)$ (8)
Similarly, differentiating Eq. (7) and (5), we get: $S_4(\lambda) - S_2(\lambda) = F_{90°}(\lambda)$ (9)
Finally, we retrieve the Raman signal R by applying Eq. (2):

$$R(\lambda) = S_3(\lambda) - S_1(\lambda) - ratio(\lambda) \cdot \left(S_4(\lambda) - S_2(\lambda)\right) \quad (10)$$

The sequence of operations is described in Figure 5. The PC algorithm is effective for the detection of O_2, N_2, CO, CO_2 and H_2O. However, this algorithm leads to a resulting H_2 signal that is only one-fourth the main parallel H_2 signal. Therefore, we had to implement the usual background subtraction algorithm as a complement to the PC algorithm.

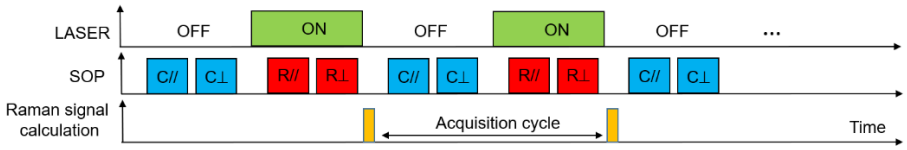

Figure 5. ***Chronogram of readout cycle in presence of strong Cerenkov perturbation (PC algorithm)***

Algorithm #2: Background Subtraction (BS)

This second algorithm is often used in spectrometry with CCD detectors. It does not involve polarization correction, nor laser tuning. The principle consists in recording the signal spectrum and interpolating a background signal from reference points A and B (respectively located out of the band, at wavelengths λ_A and λ_B). As an example, see Ref #1 and Ref #2 in Figure 3.

The interpolation function is determined beforehand in laboratory from a mixture that does not contain the gas to be detected. The interpolation function is usually of polynomial form. We choose a second-order polynomial that involves three calibration constants: a, b and λ_{ref}, this latter parameter determining the shape of the parabolic function that best fits the background (BG) shape as follows:

$$BG\ (\lambda_A) = a + b * (\lambda_A - \lambda_{ref})^2 \qquad (12a)$$

$$BG\ (\lambda_B) = a + b * (\lambda_B - \lambda_{ref})^2 \qquad (12b)$$

We get the constants a and b by subtracting Eq. (12a) to Eq. (12b): $b = \frac{BG\ (\lambda_B) - BG\ (\lambda_A)}{[\lambda_B{}^2 - \lambda_A{}^2] + 2 \cdot \lambda_{ref} \cdot (\lambda_A - \lambda_B)}$ (13)

Finally, the value of a is obtained from either Eq. (12a) or Eq. (12b).

5. RAMAN CALIBRATION IN AIR, CO, CO_2 AND H_2

Preliminary tests were performed in CEA LIST laboratory in ambient air. Then, the Raman probe and the rack were moved to CNRS-ICARE facility (Orléans, France) to perform additional calibrations on a dedicated gas cell (NC2V) with CO, CO_2 and H_2 gas.

5.1. Preliminary experiments in laboratory

An example of Raman spectrum in ambient air (78 % N_2, 21 % O_2) is shown in Fig. 6.

The readout time was 10 seconds (readout noise ~ 264 kCts/pix). The laser power was 1 W (160 mW at focal point) and the exposure time was 600 s (60 x 10 seconds).

Compared to the first compact probe [16], the Raman efficiency of the new probe is higher by a factor of 17, in spite of higher internal optical losses due to polarization-induced loss by the PBS and Fresnel reflections by additional components.

The sensitivities are 12.8 kCts/% ± 1 and 7.5 kCts/% ± 1 for O_2 and N_2 respectively, from which we obtain normalized sensitivities of 6100 Cts/s.W and 2800 Cts/s.W for O_2 and N_2 respectively.

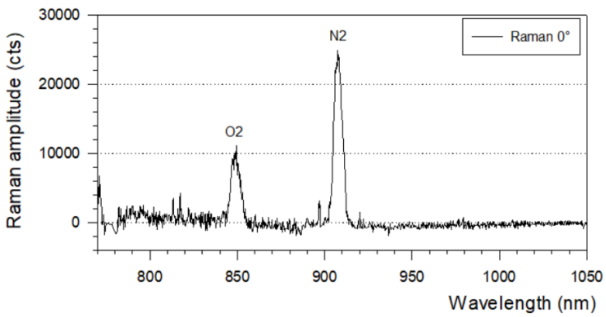

Figure 6. ***Example of Raman spectrum obtained in ambient air (1 W, 600 s) with the new probe (SOP 0°)***

Using the BS algorithm, the Signal-to-Noise Ratio (SNR) of the Raman signal is as follows [16]:

$$SNR = \frac{S}{\sqrt{S + 2 \cdot N}} \qquad (14)$$

where S is the useful Raman signal and N is the background noise. The factor of 2 arises from the operation of subtraction of the raw signal (S + N) with the background noise (N).

The SNRs are respectively 48 and 104.5 for O_2 and N_2 respectively (600 s, 160 mW at focus). The LoDs (Limit of Detection) are 1.3% and 2.2% for O_2 and N_2 respectively, for SNR = 3 at 1-σ.

5.2. Calibrations in NC2V gas cell

5.2.1 Description of the experiment

The Raman probe was placed aside to an existing gas cell (NC2V, CNRS-ICARE, Orléans, France) equipped with an optical window, shown in Fig. 7. It is a steel cylinder equipped two 10-mm thick polycarbonate (PC) windows (200 mm in diameter) at both sides.

One PC window was machined to accommodate a 1-inch, 6-mm thick fused silica window that was epoxy-bonded in the retainer. The Raman probe was then placed next to the PC window to focus inside the gas volume, away behind the glass window. To achieve this, it was thus necessary to remove the Brewster window out of the Raman probe. In turn, part of the Raman light is reflected at both window surfaces (at normal incidence) which causes optical interference and slight oscillations in the spectra (N.B. those perturbations are not observed when the Brewster window is used).

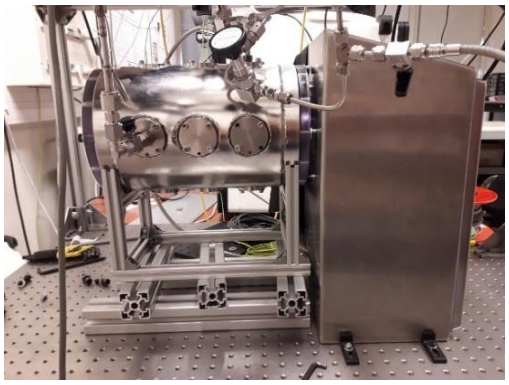

Figure 7. ***Raman probe placed aside to the NC2V gas cell (CNRS-ICARE, Orléans, France)***

The NC2V cell is connected to a vacuum pumping system, a Pirani pressure gauge, and injection lines through a valve. Preliminary to each experiment, the cell is vacuumized in order to avoid gas stratification. Ultrapure gases (99.999%) are then filled up at the desired partial pressure.

5.2.2 Calibration in air

Figure 8 shows the Raman spectra obtained in ambient air (1 atm) for both SOPs.

They are superimposed over internal fluorescence from the optical components. Raman peaks of O_2 and N_2 are effectively retrieved by application of the PC algorithm. While interference oscillations are not visible on raw spectra, they are visible on the restituted Raman spectrum and complicate the quantitative analysis.

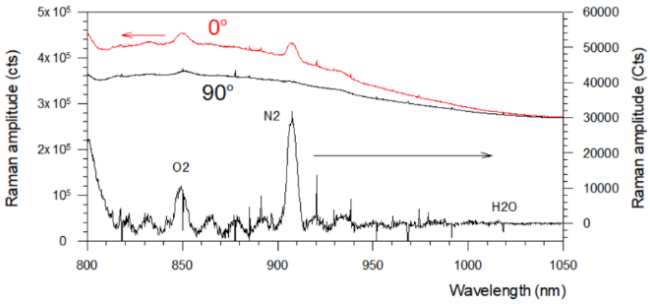

Figure 8. ***Raman spectrum of ambient air recovered by using the PC algorithm (1 W, 600 s)***

In the following, only the BS algorithm was applied with the aim to estimate the Raman detection efficiency of H_2, CO, and CO_2 with this new probe.

5.2.3 Calibration of H_2

This calibration was performed twice (with 50%-50% H_2-N_2 and 50%-50% H_2-CO mixtures).

Raman light from the silica window mainly extends up to 600 cm^{-1}, thus interfering partly with the rotational Raman S_1 band of H_2. (587 cm^{-1}).

Fortunately, the Raman contribution from the silica window remains highly polarized. Consequently, it is strongly attenuated in the 90° SOP contribution of the H_2 Raman band (with respect to the 0° contribution). Therefore, all H_2 Raman spectra were recorded on the 90° SOP.

The partial pressure of H_2 was adjusted between 0 and 10% atm (1% atm, 2.3% atm, 4.9% atm and 10.4% atm). The BG-corrected Raman spectra for the H_2 rotational line are shown in Figure 9 (λ_{ref} = 798.9 nm). The sensitivities are 16 kCts/% ± 1 (50% H_2-50% CO) and 14 kCts/%± 1 (50% H_2-50% N_2). The LoDs (SNR=3 at 1-σ) are 1.1% atm (H_2-CO) and 1.4% atm (H_2-N_2).

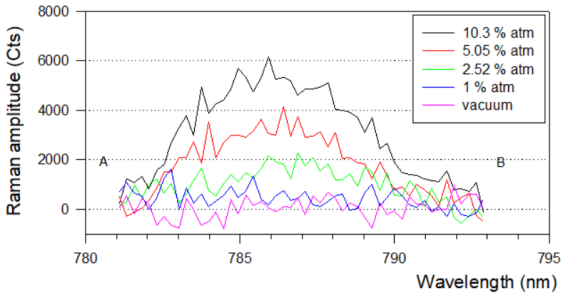

Figure 9. ***Rotational Raman spectra of H_2 in the 90° SOP (BG corrected)***

5.2.4 Calibration for CO_2

A 100% CO_2 canister was used for this test. Unlike with H_2, we recorded the Raman signal of CO_2 in the 0° SOP of the polarizer. The partial pressures were 0 atm, 5.2% atm, and 10.2% atm. Figure 10 shows the BG-corrected Raman spectra of CO_2 using the BS algorithm (λ_{ref} = 860 nm). The doublet is clearly visible. The CO_2 sensitivity is 34 kCts/%± 2 and the LoD is 1.3% atm (SNR = 3 at 1-σ).

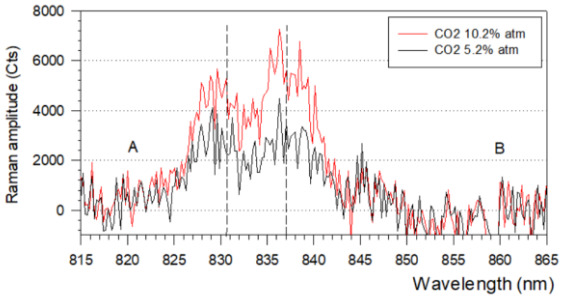

Figure 10. ***Raman spectra of CO_2 in the 0° SOP (BG-corrected)***

5.2.5 Calibration for CO

A 50% H_2-50% CO canister was used for this last experiment. The partial pressures were 0 atm, 2.5% atm, 5.05% atm, and 10.3% atm. Figure 11 shows the BG-corrected Raman spectra for CO using the BS algorithm (λ_{ref} = 885 nm). Error bars are indicated at 2-sigma. The CO sensitivity is 11 kCts/% ± 1 and the LoD is 2.5% atm (SNR = 3 at 1-σ). The sensitivity for CO detection is worse than that for CO_2 because the Raman cross-section of CO is less and only one vibration mode is involved (whereas two modes are involved for CO_2). The response curves for all gases are plotted onto Figure 12.

The concentration is the partial pressure normalized to atmospheric pressure (~1000 mbar). CO_2 exhibits the highest sensitivity due to the doublet integration.

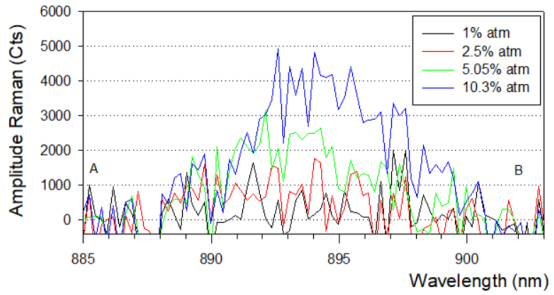

Figure 11. ***Raman spectra of CO in the 0° SOP (BG corrected)***

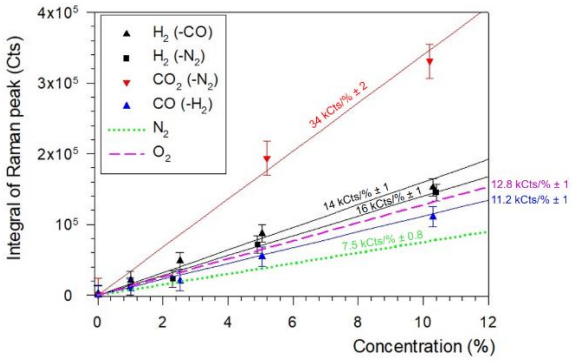

Figure 12. ***Evolution of integral of Raman peaks vs concentration (% atm) for O_2, N_2, CO, CO_2 and H_2.***

6. EXPERIMENTS IN IRRADIATION CELL (IRMA, IRSN)

6.1. Description of the irradiation experiment

The Raman probe was finally tested in an irradiation cell in order to check both the RIA influence and the algorithms for Cerenkov removal. The IRMA cell is an irradiation facility located at CEA/Saclay, France (IRSN/SERAC). Four ^{60}Co sources (Ø = 10 mm, 450-mm long) are stored into a lead case, extracted by remote manipulator, and accurately placed onto cylindrical supports by visual control though a lead glass window. The total activity (4 sources) was 580 TBq (15662 Ci) at the time of the experiment (July 2022).

For this experiment, Low-OH FIP-400 and FIP-600 fibers (Polymicro) were used. Both laser and Raman fibers were pulled inside the cell through a hole (accessible on top of the wall), winded onto a starlike support and then eventually connected to the Raman probe (Fig. 13).

The Raman probe was placed next to the starlike support (one-meter away from the support center), inserted into a box, and covered with a dark blanket. The Brewster window was again removed for this experiment. We aimed at delivering a maximum dose rate of 1 kGy/h, obtained with a source-to-fiber distance of about 30 cm. Both fibers were then winded along a circle (61 cm in diameter), delimited by plastic clamps. The total length of winded fiber was 6.7 meters (3 turns and a half). The excess fiber (~ 3 m long) was exposed as well, but to a lesser extent due to the greater distance from the source.

Figure 13. ***View of Raman probe and fiber deployment within the IRMA irradiation cell (the sources are placed at the center of the starlike support)***

Furthermore, internal fiber connections (inside the probe) were also exposed (80 cm). In the end, the equivalent length of exposed fiber was about 10 meters.

According to this configuration, the dose rate has been estimated by IRSN (MicroShield software) for four distinct source configurations, as follows: #1: 250.5 Gy/h (one source), #2: 512.9 Gy/h (two sources), #3: 843.9 Gy/h (two sources), #4: 1016.1 Gy/h (three sources). As a dose reference, we fixed a diamond ionization chamber (PTW-Freiburg) along the circular isodose. The dose rate delivered onto the fibers is approximately 4.4 times that onto the probe.

6.2. Recording of Cerenkov and fluorescence spectra

We first record the Cerenkov signal for the maximum dose rate (1 kGy/h) by using the same readout time as for ICARE (10 s). We had to reduce the readout time to 2 seconds to avoid saturation. The number of readouts increased correlatively (300 readouts for a 600-second integration time) and so did the readout noise (1.32 MCts/pix).

Preliminary to the irradiation experiment, and several times during the irradiation test, we also recorded both 0° and 90° Raman spectra of ambient air, without sources (no radiation). These reference spectra serve to calculate the ratio function during the course of the experiment, and to account for potential change due to RIA. Finally, according to the protocol described in Figure 5, both Cerenkov and Raman spectra stemming out the Raman collection fiber were alternatively recorded for each SOP. The laser power was 3.5 W (560 mW at focus).

In Figure 14a, Cerenkov spectra are shown at the beginning of the experiment for several dose rates, 0° SOP, and 120-s integration time (the Cerenkov spectra recorded on the 90° SOP are very similar and are not shown here).

Figure 14b shows the amplitude of the Cerenkov light (@800 nm) which is perfectly linear with respect to dose rate. As previously demonstrated in earlier works [19], the Raman collection fiber may be used as real-time distributed dosimeter inside the containment building, either in operational or accidental situations. Granted that several probes are meant to be deployed inside the containment, each fiber link may provide an average dose rate measurement around probe location. It is worthwhile noticing that the Cerenkov signal is temperature-independent (unlike scintillation signals) but must also be corrected for RIA influence, particularly in accidental conditions (see §6.5).

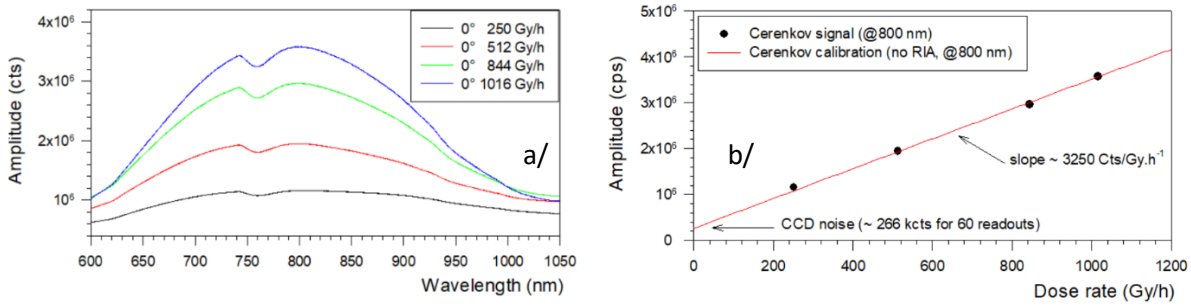

Figure 14. ***a/ Cerenkov spectra recorded for 0° SOP (120 s integration time) (not corrected for diffraction and quantum efficiencies of the spectrometer) b/ Evolution of the Cerenkov signal (@800 nm) with dose rate***

6.3. Raman recordings during the irradiation test and Cerenkov discrimination

6.3.1 Raman spectra of ambient air

We recorded Raman spectra from ambient air for the four source configurations (§6.1) for both 120 s and 600 s integration times. Figure 15a shows the raw Raman spectra flooded within broadband continuum Cerenkov and Figure 15b shows the reconstituted Raman spectra, successfully discriminated from Cerenkov perturbations, after application of the PC algorithm.

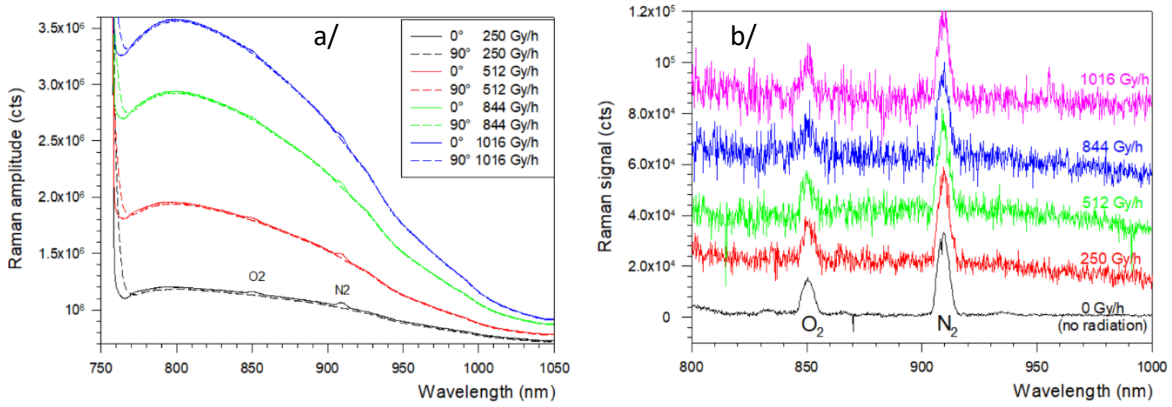

Figure 15. ***a/ Raman spectra of ambient air recorded for both 0° and 90° SOPs (60 s integration time) and b/ Cerenkov correction using the PC algorithm (data are uplifted by 20,000 cts for clarity)***

The Cerenkov signal generated by a 10-meter long collection fiber exposed to a dose rate of 1 kGy/h is found to exceed the Raman signal of O_2 (21 % atm) and N_2 (78 % atm) by factors of 187 and 63

respectively. This illustrates the challenge of performing Raman measurements in accidental conditions. The SNR (1-σ) for O_2 and N_2 detection was calculated (Eq. (14)) as a function of dose rate and the result is plotted onto Figure 16.

The data are accurately fitted by an inverse square law dependence written as follows:

$$SNR = \frac{SNR^0}{\sqrt{1+\frac{\dot{D}}{\dot{D}_0}}} \quad (15)$$

where SNR^0 is the SNR without sources and $\dot{D}$ is the dose rate in Gy/h.

$\dot{D}_0$ represents a dose rate yielding a Cerenkov signal equivalent to half the Raman signal (it does not depend on integration time).

The values of $\dot{D}_0$ are 92 Gy/h and 115 Gy/h for O_2 and N_2 respectively. The ratio $\dot{D}_0$ N_2/ $\dot{D}_0$ O_2 is equivalent to the ratio of Raman cross-sections of O_2 *vs* N_2. The Figure 16 demonstrates that the new probe now complies with the MTDR of 1 kGy/h.

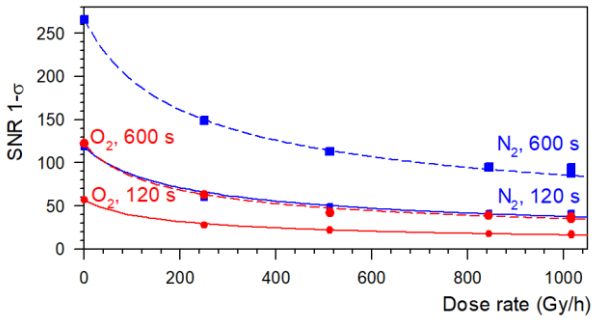

Figure 16. ***1-σ SNR of O_2 and N_2 signals with respect to dose rate (120-s and 600-s integration times).***

In accidental conditions (high dose rate), the unity term in Eq. (15) becomes negligible, so that the SNR eventually follows the following trend:

$$SNR \approx P_\ell \cdot \sqrt{\frac{t}{\dot{D}}} \quad (16)$$

where P_ℓ is laser power and t is the integration time. Laser power is therefore the main critical parameter, having the maximum impact over both SNR and LoD figures.

Eq. (16) leads to the following important conclusions:

→ Multiplying the integration time t by a factor of 4 only improves the SNR by a factor of 2.

→ Increasing laser power P_ℓ by a factor of 2 enables to discriminate Raman signals from a Cerenkov perturbation which is 4 times larger (*i.e.* a dose rate $\dot{D}$ which is 4 times larger).

6.3.2 Raman spectra of H_2-N_2 mixture contained in TEDLAR bags

We recorded Raman spectra from H_2-N_2 mixtures contained in PET-made TEDLAR bags. The first TEDLAR bag was filled with 75% H_2-25% N_2 while the second one was filled with 5% H_2-95% N_2. Each bag was placed at the output of the Raman probe, in contact with the base plate (the Brewster window was removed). Despite having focused inside the gas volume (away from the PET film), the Raman spectra are partly spoiled by the Raman emission from the PolyEthylene-Terephtalate (PET) material (highly depolarized as well).

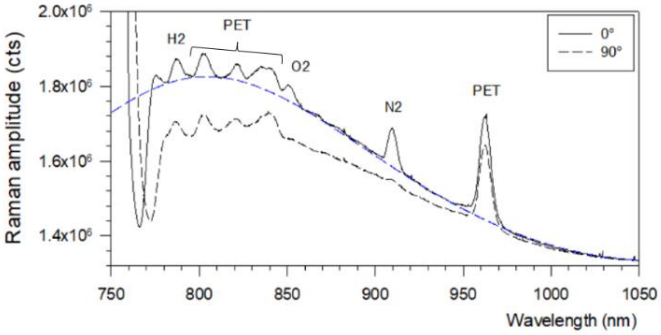

Figure 17. ***Raman spectra for both SOPs of 75% H_2-25% N_2 mixture contained in a TEDLAR bag (3.5 W, 600-s integration time). No radiation (sources removed).***

Fortunately, the H_2 Raman band does not come in interference with the Raman bands from the PET (Cf. Figure 17). The Raman peak of O_2 is also visible because the probe is actually filled with air.
The experimental procedure consisted here again in recording Raman spectra in presence of Cerenkov and fluorescence signals, for both SOPs. We applied the BS algorithm to both SOPs of H_2 Raman signals on account on high depolarization.
In Figure 18, only the 90° SOP contribution is shown (the 0° SOP contribution is similar).
Figure 19 depicts the Raman spectra of H_2, after application of the BS algorithm, with and without radiation (250 Gy/h). The H_2 band is strongly degraded but still observable.

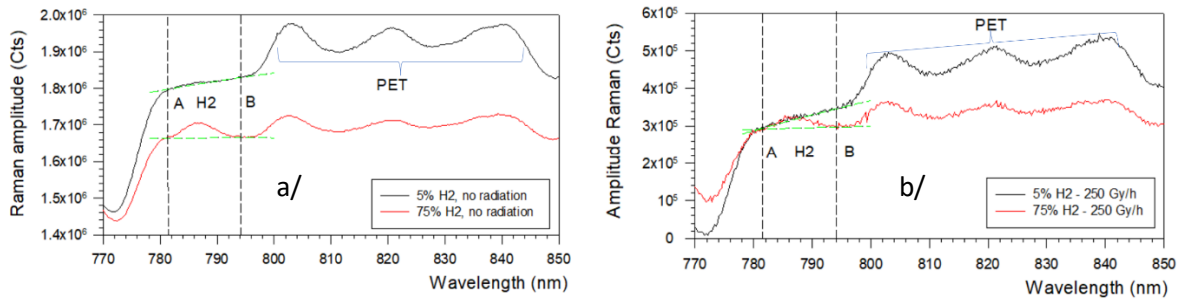

Figure 18. Raman spectra of 75% H_2-25% N_2 and 5% H_2 – 95% N_2 mixtures contained in TEDLAR bags, for the 90° SOP, without radiation (a/) and exposed to a dose rate of 250 Gy/h (b/)

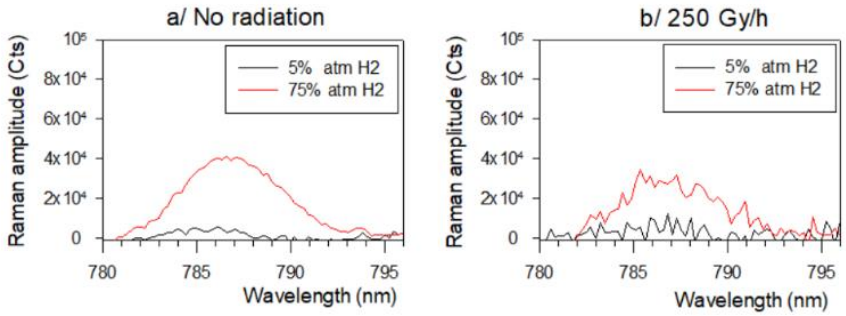

Figure 19. Background-corrected Raman spectra of 75% H_2-25% N_2 and 5% H_2 – 95% N_2 mixtures contained in TEDLAR bags: a/ no radiation, b/ exposed to a dose rate of 250 Gy/h (90° SOP).

6.4. Raman recordings during the course of the irradiation test (sources removed)

The Raman spectra were recorded several times during the experiment in order to assess probe functionality under radiation. For each recording, the accumulated dose (over the isodose) was estimated from the diamond dosimeter. The dose accumulated at the end of the experiment was 184 kGy on fibers (42 kGy on the probe). Figure 20a shows the Raman spectra of ambient air while sources are removed. The ratio function was then calculated and displayed on Figure 20b.
The ratio function is reaching stability after 22 kGy, which suggests that a predose of same order would be necessary to stabilize the spectral response. For dose higher than 22 kGy, linear adjustments are found to satisfactorily fit the ratio function.
The experiment was conducted in summer and the air temperature in the cell was 30°C, which gives a saturating water vapor pressure of about 42.4 hPa (42.4 mbar, 4.2 % atm). The Relative Humidity (RH) content was not measured, but likely to be around 70 % to 80 %, so the water vapor pressure is estimated around 3 % atm, which is of same order as the LoD for water vapor. The Raman signal of

H_2O is hardly visible on Figure 20a because the quantum efficiency of silicon dramatically drops in this spectral domain (~ 5% @1030 nm).

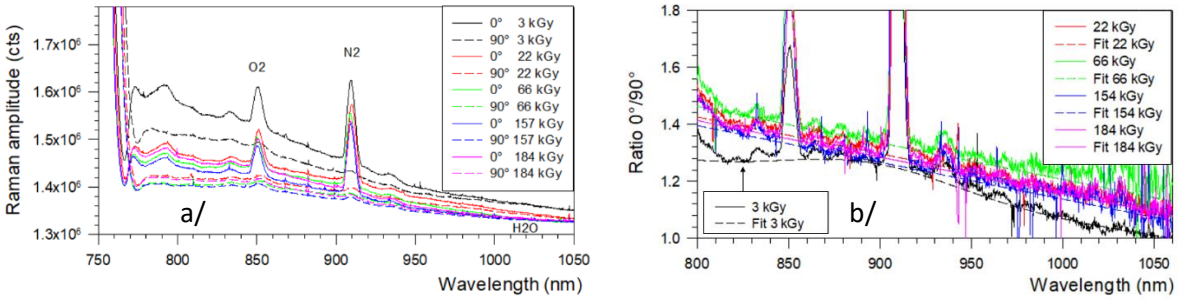

Figure 20. a/ Raman spectra of ambient air recorded for 0° and 90° polarization orientations (600 s readout time), b/ Evolution of the ratio function during irradiation

6.5. RIA evolution

The RIA has two contributions: transient (during irradiation) and permanent (after irradiation). Anhydroguide fibres mainly exhibit transient RIA, which means that the RIA is maximum during irradiation and recovers significantly several hours after irradiation. Previous experiments performed with low-OH fibres (OFS) onto the POSEIDON irradiation cell (CEA/Saclay) [16] led to the conclusion that a constant attenuation was reached after 24 hours, up to 1.6 MGy. The transient RIA was 0.35 dB/m (@800 nm) and 0.25 dB/m (@850 nm) within the Raman band. For a 10-meter long fiber, the maximum attenuation during accidental conditions is expected to be about -3 dB. This signal loss requires increasing the laser power by a factor of two in order to compensate for it.

We made similar observations during the IRMA experiment with a FIP-400 fiber. The RIA observed was less than 0.25 dB/m in the Raman range for a total dose of 184 kGy.

Figure 21 shows the evolution with dose of the pressure of O_2 and N_2 as calculated from Raman spectra. As the RIA is growing with accumulated dose, both laser power and Raman signals transmitted through the fibers are progressively attenuated, therefore leading to a drift in the calculated pressure. Both O_2 and N_2 pressures are actually underestimated.

Several hours after irradiation, the transmission recovers and the Raman-inferred pressures thus tend to converge to the real pressure values (78% atm N_2 and 21% atm O_2). It is worthwhile noticing that the drift is also partly reduced when considering alternate calibration after predose (22 kGy).

To compensate for RIA-induced drift in Raman-inferred pressures, internal Raman reference are thus required to correct for changes in the calibration parameters in real-time. To achieve this, a foreign material is often incorporated into the probe.

The Raman light emitted by this reference material is superimposed onto the gas Raman signal and serves as amplitude reference. The most suitable solution in the case of the MITHYGENE probe is to purge the inner volume with a reference gas (for instance methane, providing an additional Raman peak at 960 nm (2918 cm^{-1})).

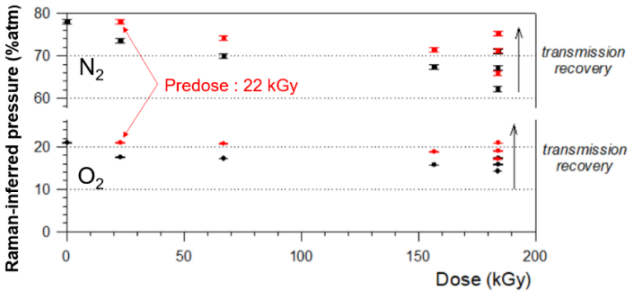

Figure 21. Evolution of Raman-inferred pressure of O_2 and N_2 with accumulated dose

7. CONCLUSIONS

During a severe nuclear accident, leading up to core melting, reaction of core constituents with coolant water and Molten Corium-Concrete Interaction (MCCI) both release large amounts of hydrogen (H_2) and carbon monoxide (CO) combustion gases in the containment atmosphere. Depending on local partial pressures of H_2, air (21% O_2, 78% N_2) and water vapor (H_2O), according to Shapiro's ternary diagram, deflagration and detonation may occur with potential deleterious impact over equipments and structures. Passive Autocatalytics Recombiners (PARs) only provide partial mitigation and does not accurately assess the H_2-risk.

As an improvement in the H_2-risk management strategy, CEA LIST, IRSN and ARCYS have designed, assembled and tested a fiber-coupled nuclearized Raman gas prototype probe, within the framework of the European MITHEGENE Project. The H_2-risk may be assessed through the multipoint monitoring of H_2, O_2, N_2 and H_2O, associated with localization onto the Shapiro-Moffette diagram. Furthermore, the monitoring of additional gases such as CO and CO_2 provides complementary information about the progression of MCCI.

Spontaneous Raman Scattering conveys many other decisive advantages: simplicity, flexibility, chemical-selectivity, distributed and local gas detection (~ cm^3). Furthermore, fiber-coupled Raman gas probes may be shock- and vibration-proof and radiation-hardened. As any instrumentation operating in NPPs, the Raman probe must be qualified *vs* seismic risk. Finally, a spectrometric readout unit is placed away from the radiological perimeter, fiber-connected to the Raman probes located inside the containment with optical fiber cables (10- to 20-m long). SA-qualified optical penetrations are commercially available and may be implemented in substitution to existing electrical ones.

In view of a proof-of-concept, the Raman probe is fiber-coupled to a single laser (@750 nm, 3.5 W) and a Charge-Coupled Device (CCD)-based imaging spectrometer. Compared with the previous single-pass transverse probe [16], this new probe is inserted into a sealed case (IP69K), that will be further equipped with an Anti-Fogging and Anti-Aerosol (AF-AA) module that protects the optical interface from contamination and water condensation. Furthermore, the probe is equipped with a remotely controlled polarization rotation device in order to provide Raman spectra for both polarization states (polarization-diversity receiver). The probe also integrates two optical penetration assemblies allowing for laser input and Raman signal output as well as electrical connections providing Joule heating and signal command for a rotating actuator. Emergency power supplies may potentially power this unit, in case of power outage (as it happened during the Fukushima Daiichi's accident). The power consumption is estimated to be about 15 kWh (3-hour intense Joule heating followed by 3-day continuous operation), representative of a conventional Li-ion battery for electric car.

We obtained Raman spectra of air, water vapor, hydrogen, carbon monoxide and carbon dioxide in laboratory conditions. Due to limited time and budget, the Raman probe was placed aside to an existing gas cell (NC2V, CNRS-ICARE) equipped with an optical window. For this test, we had to remove the Brewster window off the Raman probe. A representative test would be to enclose the probe into a large dedicated cell in which the gases are flown at the required pressure.

Additional SA-qualified temperature sensors will be mandatory in order to retrieve partial pressures of all gases. Each probe would incorporate a temperature sensor close to (or embedded into) each AF-AA module. Without radiation, the Limit of Detection (LoD) for all gases is typically of several percents for a laser power of 1 W (160 mW at focus) and a response time of 10 minutes. A notable exception is H_2O, which is hardly detected on account on the low quantum efficiency of silicon in this extreme part

of NIR Raman spectrum. Therefore, the partial pressure of H_2O would be most likely determined by subtracting the total pressure measurement (obtained from the control-command of the NPP) to the sum of Raman-inferred partial pressures of all other gases.

The RIA is kept below 0.35 dB/m (@800 nm) and 0.2 dB/m (@900 nm) for a total dose of 1.6 MGy, leading to additional losses of 3.5 dB (@800 nm) and 2 dB (@900 nm) over an exposed fiber length of 10 meters. In accidental conditions, under a dose rate as high as 1 kGy/h, the most detrimental phenomenon appears to be the Cerenkov light stemming from the fiber used for Raman collection. The Cerenkov light superimposes over the useful Raman signal thus degrading both Signal-to-Noise Ratios (SNRs) and LoDs. The Cerenkov perturbation is typically 2 to 3 orders of magnitude larger than the useful Raman signal. We applied two algorithms to discriminate Raman signals out of Cerenkov perturbations: Background Subtraction (BS) and Polarization Correction (PC). The PC algorithm pertains to O_2, N_2, CO and CO_2 monitoring while the BS algorithm was applied to the monitoring of the 90° SOP of the rotational band of H_2 on account on its high depolarization. The SNR follows an inverse square law dependence with respect to the dose rate. As an example, without radiation, the LoDs (SNR = 3) for O_2 and N_2 are about 0.5% and 0.9% respectively (10-minutes, 560 mW at focus). Under a dose rate of 1 kGy/h, they are degraded down to 1.8% and 2.7% respectively. The LoDs (SNR = 3) for H_2 are estimated to be 2% (0 kGy/h) and 6.5% (1 kGy/h).

Laser power is the most critical parameter ruling both the SNRs and LoDs. There is room for improvement because the input polarizer generated excessive loss as it was used out of specification (design wavelength ~780 nm) and lasers that are more powerful are available on the market. In the future, we will have to increase the laser power at focus by at least a factor of four (*i.e.* 2 W at focus) in order to improve the LoD on H_2, to comply with SAMGs (5-minute integration time) and finally, to compensate for Radiation-Induced Attenuation (RIA). At such power, no ignition risk is expected and the MITHYGENE probe is ATEX-compatible.

The Mithygene Project ends up with a proof-of-concept of Raman probe prototype dedicated to MCCI/H_2-risk management during severe accidents. We estimate the Technological Readiness Level (TRL) of the prototype probe to be about 5 to 6.

Further developments would involve the design of a prototype probe with fixed optics (for instance, bonded with high-temperature epoxy onto the support base). This new prototype probe will then be submitted to shock/vibration tests according to seismic standards [IEC 60068]-[IEC 60980]. Then, the prototype probe (equipped with its Brewster window, its AF-AA module and a temperature sensor) will have to be tested into a large dedicated gas cell in which the gases are flown at required pressures and in a radiation cell, according to a setup similar to the IRMA experiment.

8. ACKNOWLEDGEMENTS

The MITHYGENE project was coordinated by the French ANR (*Agence Nationale de la Recherche*), partly funded by the PIA-RSNR (*Programme d'Investissements d'Avenir, Recherche en Sûreté Nucléaire et Radioprotectio*n) of the French government, and was also partly financially supported by two French companies: EDF and AIR-LIQUIDE.

We thank Stéphane Poirier and Hortense Desjonquères (IRSN) for their help in conducting the IRMA experiment and providing us with the starlike support, and Mahmoud Idir and Sharat Nagaraju (CNRS-ICARE) for operating the NC2V gas cell.

9. REFERENCES

[1] IAEA, “Mitigation of hydrogen hazards in severe accidents in nuclear power plants,” TECDOC N° 1661, Vienna, 2011.

[2] D. Jacquemain, in “Nuclear power reactor core melt accidents – current state of knowledge,” *EDP Sciences*, 2015.

[3] V.G. Petrosyan, E.A. Yeghoyan, A.D. Grigoryan, A.P. Petrosyan, M.R. Movsisyan, “Characteristics of hydrogen monitoring systems for severe accident management at a Nuclear Power Plant,” *Thermal Eng.,* 65 (2), 2018, pp. 79-87.

[4] A. Bentaïb, N. Meynet and A. Bleyer, “Overview on hydrogen risk research and development activities: methodology and open issues,“ *Nucl. Eng. Technol.,* vol. 47, pp. 26-32, 2005.

[5] A. Omoto, “The accident at TEPCO’s Fukushima-Daiichi Nuclear Power Station: What went wrong and what lessons are universal?,“ *Nucl. Instr. Methods,* A, vol. 731, pp. 3-7, 2013.

[6] Z.M. Shapiro and T. R. Moffette, “Hydrogen flammability data and application to PWR Loss-Of-Coolant Accident,” *WAPD--SC-545*, 4327402, Pittsburgh, PA, 1957.

[7] A. Hill, “Multi-functional containment atmosphere monitoring,” *NUSSA Workshop*, Sept. 7-8, 2012, Beijing, China.

[8] T. Hübert, L. Boon-Brett, G. Black and U. Banach, “Hydrogen sensors – a review,” *Sens. Actuators, B*, vol. 157, pp. 329-352, 2011.

[9] A. Campargues, S. Kassi, K. Pachucki and J. Komosa, “The absorption spectrum of H_2:CRDS measurements of the (2-0) band, review of the literature data and accurate *ab initio* line list up to 35 000 cm^{-1},” *Phys. Chem. Chem. Phys.,* vol. 14, pp. 802-815, 2012.

[10] D.A. Long, The Raman effect, Wiley & Sons, 2002.

[11] H.W. Schrötter and H.W. Klöckner, Ch. 4, “Raman scattering cross sections in gases and liquids,” pp. 123-164, in “Raman Spectroscopy of gases and liquids,” Ed. By A. Weber, *Topics in Current Physics*, Springer-Verlag, 1979.

[12] W.F. Murphy, W. Holzer and H.J. Bernstein, “Gas-phase Raman intensities: A review of ‘pre-laser’ data,” *Appl. Spectrosc.,* vol. 23, n°3, pp. 211-218, 1969.

[13] D.G. Fouche and R.K. Chang, “Relative Raman cross-section for O_3, CH_4, C_3H_8, NO, N_2O and H_2,” *Appl. Phys. Lett.,* vol. 20, n°7, 1972, pp. 256-257.

[14] W.R. Fenner, H.A. Hyatt, J.M. Kellam and S.P.S Porto, “Raman cross section of some simple gases,” *J. Opt. Soc. Am.,* vol. 63, n°1, pp. 73-77, 1973.

[15] D.V. Petrov, I.I. Matrosov, A.R. Zaripov, A.S. Maznoy, “Effects of pressure and composition on Raman spectra of CO-H_2-CO_2-CH_4 mixtures,” *Spectrochimica Acta A*, vol. 215, 2019, pp. 363-370.

[16] S. Magne, S. Nehr, X. Buet, A. Bentaib, E. Porcheron, R. Grosseuvres, E. Studer, R. Scarpa, D. Abdo, J-L. Widloecher, O. Norvez, N. Chaumeix, J. Dhote, M. Freyssinier, A. Ruffien-Ciszak, “In situ gas monitoring by Fiber-Coupled Raman Spectrometry for H_2-risk management in nuclear containment during a severe nuclear accident,” *IEEE Trans. Nucl. Sci.*, vol. 67, n°4, pp. 617-624, 2020.

[17] J. Kiefer, T. Seeger, S. Steuer, S. Schorsch, M.C. Weikl and A. Leipertz, “Design and characterization of a Raman-scattering-based sensor system for temporally resolved gas analysis and its application in a gas turbine power plant,” *Meas. Sci. Tech.,* vol. 19, 085408, 2008.

[18]A. Kumamoto, H. Iseki, R. Ono, T. Oda, “Measurement of minimum ignition energy in hydrogen-oxygen-nitrogen premixed gas by spark discharge,” *J. Phys.: Conf. Ser.* 301, vol. 12039, 2011.

[19]B. Brichard, A.F. Fernandez, H. Ooms, F. Berghmans, “Fibre-optic gamma-flux monitoring in a fission reactor by means of Cerenkov radiation,” *Meas. Sci. Technol.,* vol. 18, pp. 3257-3262, 2007.

[20]M.J. Marrone, “Radiation-induced luminescence in silica core optical fibers,” *Appl. Phys. Lett.,* 38 (3), pp. 115-117, 1981.

[21]S. Girard, J. Kuhnhenn, A. Gusarov, B. Brichard, M. Van Uffelen, Y. Ouerdane, A. Boukenter, and C. Marcandella, “Radiation Effects on Silica-Based Optical Fibers: Recent Advances and Future Challenges,” *IEEE Trans. Nucl. Sci.,* vol. 60, n°3, pp. 2015-2036, 2013.

[22]M.P. Kissane, “On the Nature of Aerosols Produced during a Severe Accident of a Water-Cooled Nuclear Reactor,” *Nucl. Eng. Des.,* vol. 238, n°10, pp. 2792–2800, 2008.

[23]E. Porcheron, L. Thause, J. Malet, P. Cornet, P. Brun, J. Vendel, “Simultaneous application of Spontaneous Raman Scattering and LDV / PIV for steam / air flow characterization,” *10th International Symposium on Flow Visualization (ISFV-11),* Kyoto, 2002.

[24]E. Porcheron, P. Lemaitre, A. Nuboer, V. Rochas and J. Vendel, Experimental investigation in the TOSQAN facility of heat and mass transfers in a spray for containment application, *Nucl. Eng. Des.*, vol. 237, pp. 1862-1871, 2007.

[25]H. Sun, E. Porcheron, S. Magne, M. Leroy, J. Dhote, A. Ruffien-Ciszak, A. Bentaïb, “Experimental investigation on Fiber-Coupled Raman spectrometry in presence of aerosols : application for reactor containment gas detection in severe accident conditions,” *SAMMI-2020, OCDE/NEA Specialist workshop on Advanced Measurement Methods and Instrumentation for Enhancing Severe Accident Management in NPP addressing Emergency, Stabilization and Long-Term recovery Phase*, December 7-10, 2020, Fukushima, Japan.